Advances in Water Resources 95 (2016) 176–189

Contents lists available at ScienceDirect

Advances in Water Resources

journal homepage: www.elsevier.com/locate/advwatres

Intercomparison of 3D pore-scale flow and solute transport simulation methods

Xiaofan Yang[a], Yashar Mehmani[b], William A. Perkins[a], Andrea Pasquali[c], Martin Schönherr[c], Kyungjoo Kim[d], Mauro Perego[d], Michael L. Parks[d], Nathaniel Trask[e], Matthew T. Balhoff[f], Marshall C. Richmond[a], Martin Geier[c], Manfred Krafczyk[c], Li-Shi Luo[g,h], Alexandre M. Tartakovsky[a], Timothy D. Scheibe[a,*]

[a] Pacific Northwest National Laboratory, PO Box 999, MS K9-36, Richland, WA 99352, United States
[b] School of Earth, Energy and Environmental Sciences, Stanford University, 397 Panama Mall, Mitchell Building 101, Stanford, CA 94305-2210, United States
[c] Institute for Computational Modelling in Civil Engineering, Technische Universität Braunschweig, Pockelsstr. 3, Braunschweig 38106, Germany
[d] Sandia National Laboratories, PO Box 5800, Albuquerque, NM 87185, United States
[e] The Division of Applied Mathematics, Brown University, 182 George St., Providence, RI 02906, United States
[f] Department of Petroleum and Geosystems Engineering, University of Texas at Austin, 200 E. Dean Keeton St., Stop C0300, Austin, TX 78712-1585, United States
[g] Department of Mathematics and Statistics, Old Dominion University, Engineering & Computational Science Building, 4700 Elkhorn Ave., Norfolk, VA 23529, United States
[h] Beijing Computational Science Research Center, Beijing 100094, China

ARTICLE INFO

Article history:
Available online 28 September 2015

Keywords:
Pore-scale modeling
Porous media flow
Computational fluid dynamics
Lattice Boltzmann method
Smoothed particle hydrodynamics
Pore-network model

ABSTRACT

Multiple numerical approaches have been developed to simulate porous media fluid flow and solute transport at the pore scale. These include 1) methods that explicitly model the three-dimensional geometry of pore spaces and 2) methods that conceptualize the pore space as a topologically consistent set of stylized pore bodies and pore throats. In previous work we validated a model of the first type, using computational fluid dynamics (CFD) codes employing a standard finite volume method (FVM), against magnetic resonance velocimetry (MRV) measurements of pore-scale velocities. Here we expand that validation to include additional models of the first type based on the lattice Boltzmann method (LBM) and smoothed particle hydrodynamics (SPH), as well as a model of the second type, a pore-network model (PNM). The PNM approach used in the current study was recently improved and demonstrated to accurately simulate solute transport in a two-dimensional experiment. While the PNM approach is computationally much less demanding than direct numerical simulation methods, the effect of conceptualizing complex three-dimensional pore geometries on solute transport in the manner of PNMs has not been fully determined. We apply all four approaches (FVM-based CFD, LBM, SPH and PNM) to simulate pore-scale velocity distributions and (for capable codes) nonreactive solute transport, and intercompare the model results. Comparisons are drawn both in terms of macroscopic variables (*e.g.*, permeability, solute breakthrough curves) and microscopic variables (*e.g.*, local velocities and concentrations). Generally good agreement was achieved among the various approaches, but some differences were observed depending on the model context. The intercomparison work was challenging because of variable capabilities of the codes, and inspired some code enhancements to allow consistent comparison of flow and transport simulations across the full suite of methods. This study provides support for confidence in a variety of pore-scale modeling methods and motivates further development and application of pore-scale simulation methods.

1. Introduction

Flow and transport processes in porous media have been intensively studied because of their importance in numerous industrial, biological, and environmental applications [1]. Pore space geometry and topology are key factors that influence flow and transport phenomena through porous media, but the complexity and small scale of natural pore geometries renders it challenging to both measure and simulate pore-scale flow and transport processes. Accordingly, mathematical models have traditionally been developed at macroscopic scales that do not explicitly consider pore geometry [2].

---

[*] Corresponding author. Tel.: +1 509 371 7633; fax: +1 509 371 6110.
E-mail address: tim.scheibe@pnnl.gov (T.D. Scheibe).

http://dx.doi.org/10.1016/j.advwatres.2015.09.015
0309-1708/© 2015 Published by Elsevier Ltd.

Recently, because of the availability of increasingly powerful computing resources and improved pore-scale characterization methods, pore-scale modeling has become an important tool for studying complex flow and transport processes and relating them to macroscopic phenomena and is complemented by simplified representations of porous media, such as regular or random sphere packs [3–8] and physical micromodels [9]. Pore-scale models have also recently been coupled with continuum-scale models in hybrid multiscale simulations to increase the fidelity of simulation results where needed (*e.g.*, [10–14]).

Various computational methods have been developed and applied to the pore scale to study flow and transport phenomena [15–17]. Considering the complexity of the pore geometries, the first step prior to modeling is to characterize the pore space and structures. Imaging techniques such as X-ray microtomography (XMT) [18] and magnetic resonance velocimetry (MRV) measurements [19–23] have made it possible to obtain accurate 3D characterizations of the pore geometry at high resolution. Pore-scale modeling can then proceed either by simulating directly on the complex pore geometry, or on a conceptualized pore network that maintains the same topological structure. The first class of model is typically referred to as direct numerical simulation (DNS). DNS approaches include standard computational fluid dynamics (CFD) [24], lattice Boltzmann method (LBM) [25–27], and smoothed particle hydrodynamics (SPH) [28]. The second class of model represents the pore space as a network connected by geometrically simplified pore bodies and pore throats and most commonly takes the form of pore-network models (PNM) [29]. Both flow and transport processes can be represented using either of these approaches.

Computational fluid dynamics (CFD) methods use various numerical discretization methods (*e.g.*, the finite volume method, finite difference method, *etc.*) to solve the governing partial differential equations (PDEs, *e.g.*, Navier–Stokes (N–S) equations for incompressible flow). Their use in pore-scale modeling requires generation of a structured or unstructured numerical mesh describing the pore geometry. Recently, Yang et al. [30] used finite volume method (FVM)-based CFD techniques to solve the Navier–Stokes flow equations in a monodispersed sphere pack and successfully compared the pore-scale flow field with magnetic resonance velocimetry (MRV) measurements, which provided insightful information to improve both the pore-scale modeling approach and the MRV experimental methods. The CFD-based pore-scale simulation studies have demonstrated the potential utility of numerical simulations and provided preliminary validation of their equivalence to experimental observations.

The lattice Boltzmann method (LBM) is a particle-based numerical approach that is well suited to solving pore-scale flow equations since its strength lies in the ability to easily represent complex physical phenomena in irregular geometries using simple Cartesian grids. It has been successfully used in the study of flow in porous media at the pore scale [31–34]. Pan et al. [35] quantitatively evaluated the capability and accuracy of the LBM for modeling flow through porous media. Three-dimensional flow through a body-centered cubic (BCC) array of spheres and a random-sized sphere-pack were both examined in their study. Their results demonstrated that the Multi-Relaxation-Time (MRT)-LBM model is superior to the Bhatnagar–Gross–Krook (BGK)-LBM model with only one relaxation time, and that interpolation significantly improves the accuracy of the fluid–solid boundary conditions. Recently, Khirevich et al. [36] introduced a two-relaxation-times (TRT)-LBM model and thoroughly studied its impact on the accuracy of the drag force/permeability computations with the D3Q19 velocity set in both regular and random packings of monodispersed spheres or cubics. Their research presented some recent advances in LBM and greatly helped the user community to improve the models for such applications.

The smoothed particle hydrodynamics (SPH) method is a meshfree Lagrangian particle method first proposed for astrophysical problems [37,38] and is now widely applied. A key advantage of particle methods such as SPH and LBM [33] is in their ability to advect mass with each particle, thus removing the need to explicitly track phase interfaces for problems involving multiple fluid phases or free surface flows. The computational cost of managing free particles has been mitigated by the development of new parallel hardware architectures. In contrast to the LBM, SPH directly solves discretized forms of the Navier–Stokes equations, just as do the CFD methods. Tartakovsky et al. [39] compared their SPH solution of the diffusion equation with fixed and moving reactive solid–fluid boundaries to analytic solutions and LBM simulations. Coupled three-dimensional flow, reactive transport and precipitation in a fracture aperture with a complex geometry were also successfully simulated to show the capability of the model. It also pointed out the high computational cost of the SPH model, which could be partially overcome by using parallel computing. In the more recent review of Tartakovsky et al. [40], the latest development and advantages of the SPH model used in pore-scale flow and transport studies have been discussed and summarized.

The fourth major pore-scale modeling approach considered here – the pore-network model (PNM) – conceptually represents complex pore geometries as interconnected fundamental units with simplified geometries to represent pore throats and pore bodies. This method retains the complete topology of the actual pore space but does not represent the geometric details of individual pores/throats as required by the other methods. Because the solution of PDEs for the pore-network model reduces to simultaneous solution of a set of analytical models for flow in each network element, the pore-network method is significantly less computationally demanding than the other approaches and has been successfully applied to a broad range of problem types (*e.g.*, [29,41]). Mehmani et al. [42] developed a new streamline splitting method (SSM) to more accurately simulate transport by incorporating partial mixing at the pore scale. The SSM was validated against direct simulations and micromodel experiments across a wide range of pore-structure and fluid-flow parameters. Recent modifications [42] have also improved the representation of transport physics within pore throats. A review of the PNM and its applications is provided by Mehmani and Balhoff [43].

Each pore-scale numerical approach mentioned above has strengths in areas such as accuracy, flexibility, computational speed, or scalability. Hence there is a strong benefit in intercomparing these models using benchmark problems. While each of these four methodologies has been widely applied to simulate pore-scale fluid flow and other processes, there have been relatively few systematic comparisons of these methodologies for a complex system representative of real porous media. Oostrom et al. [9] conducted a series of nonreactive solute transport experiments in pore-scale micromodels and offered the data to the pore-scale modeling community to test their numerical simulators. Five pore-scale models and one continuum-scale model were used to simulate the experiments, including a standard CFD model, LBM and PNM. Comparisons between experimental and numerical results for the four challenge experiments show that all pore-scale models were able to satisfactorily simulate the experiments. However, the comparisons in [9] are limited to simple pore-structures with regular pore space arrangement and steady-state tracer simulations. There have also been a limited number of intercomparison studies based on three-dimensional realistic pore geometries (complex pore structures imaged in high resolution). For example, Ahrenholz et al. [33] used two methods (LBM and PNM) to predict the capillary hysteresis in a porous material and cross-compared with measurements. Both simple and complex pore geometries were tested. Specifically, a realistic sand sample was scanned using X-ray tomography. Detailed pore structures were then used in the simulations of water saturation. Both methods showed their capabilities to accurately predict the water drainage at different stages and achieved excellent agreement with the experimental data.

Recently, researchers at Montana State University used high-resolution magnetic resonance velocimetry (MRV) to generate three-dimensional images of fluid flow through a randomized monodispersed sphere pack at pore-scale resolution (40 μm). The sphere pack used for MRV measurements was constructed of 6864 monodispersed polystyrene beads (Duke Scientific, Inc.) with a diameter of 500 μm. The MRV results were previously compared with FVM-based CFD models by Yang et al. [30]. The results compared very well, which inspired the extension of these validation studies to include a variety of pore-scale simulation methods, motivating the research reported here. In the current benchmark study, five computational codes embodying the four major pore-scale numerical approaches introduced above (FVM-based CFD, LBM, SPH and PNM) have been applied to the same micro-sized sphere pack simulation described in [30] . This paper describes and intercompares the results of flow and solute transport simulations among these four methodologies.

The outline of this paper is as follows: 1) the benchmark problem is introduced, including the pore geometry, flow and solute tracer conditions, and information on mesh generation methods; 2) the four major pore-scale numerical approaches are described in greater detail, including two FVM-based CFD codes, one LBM code, one SPH code and one PNM code. Information includes descriptions of the governing equations, numerical algorithms, boundary/initial conditions, mesh types and grid resolutions, computing cost and other requirements of each method; 3) results of the simulations are presented in terms of both flow field comparisons (velocities, pressure drop, *etc.*) and solute transport comparisons (breakthrough curves and dispersion analysis); and 4) a summary of conclusions is provided.

2. Benchmark problem

The benchmark problem describes fluid flow and non-reactive solute transport through a centimeter-scale column packed with 6864 random monodispersed polystyrene beads (Fig. 1). The diameter of the beads is 500 μm, and the porosity of the sphere pack is 0.4267 as measured by the MRV experiments. However, the modeled porosity is mesh-dependent and varies slightly among the various numerical simulations. The pore geometry used in the various numerical models was specified directly from the voxel data provided in the MRV geometry dataset. The centroids (locations of the sphere centers) were identified from the voxel data using an algorithm called Sphere Lociextraction through Iterative Erosion (SLIE, [30]). The dimensions of the sphere pack, the flow conditions and boundary conditions for the pore-scale simulations were specified to match the experimental conditions (Table 1). However, for CFD simulations, in order to improve numerical convergence and achieve fully-developed flow (parabolic velocity profile) prior to entry into the sphere pack, two open flow buffer regions were added to the inlet and outlet of the sphere pack. For the flow simulations, standard properties of water (density and viscosity) were applied. Initial conditions are no flow in the entire column; a transient flow simulation is performed until the system reaches a steady-state flow condition. For the boundary conditions, a fixed volumetric flow rate of 100 mL/h (2.771×10^{-5} kg/s) was employed at the inlet, consistent with experimental conditions. The outlet boundary was specified as a fixed pressure to allow flow to freely exit, matching experimental conditions. The cylindrical bounding surfaces were treated as no-slip boundaries. In some cases, based on code capabilities and to facilitate consistent intercomparisons, the specific treatment of boundary conditions was varied somewhat among different numerical approaches as described in the following sections. The Darcy flux, average pore velocity and grain-scale Reynolds number of the experimental system are listed in Table 1 and demonstrate that the flow is in the Stokes flow regime.

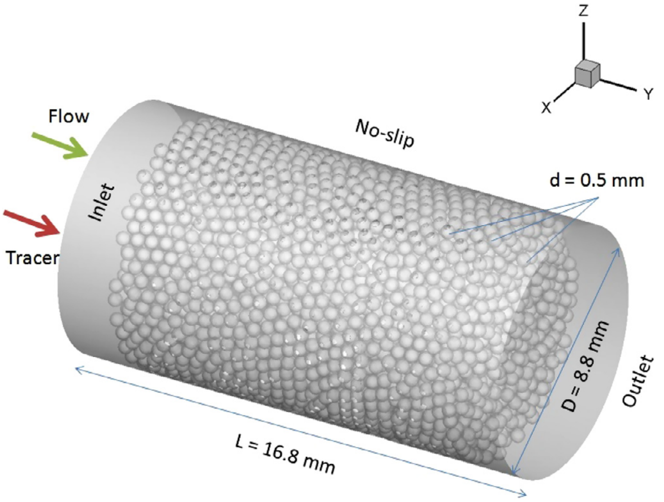

Fig. 1. Computational domain of the benchmark sphere pack problem: pore geometry, dimension and boundary conditions.

Table 1
Dimensions and parameters of the column.

Parameter	Symbol (units)		Value
Length of the simulated domain	L_c	(mm)	16.8
Length of the sphere pack	L_b	(mm)	12.8
Diameter of the column	D	(mm)	8.8
Diameter of the beads	d_p	(mm)	0.5
Porosity	ϵ		0.4267
Volumetric flow rate	Q	(kg/s)	2.771×10^{-5}
Fluid density	ρ	(kg/m^3)	997.561
Fluid dynamic viscosity	μ	(Pa s)	8.887×10^{-4}
Darcy flux	q	(m/s)	4.556×10^{-4}
Pore velocity	v_e	(m/s)	1.068×10^{-3}
Grain-based Reynolds number	Re_p		0.6
Molecular diffusion coefficient	D_m	(m^2/s)	2.08×10^{-9}
Schmidt number	Sc		428

Solute transport was not conducted in the MRV experiments, and thus was not simulated in previous work reported by Yang et al. [30]. Accordingly, solute transport simulations performed here can only be compared among various codes and methods, not with experimental observations. For the numerical simulations reported here, the solute was assumed to have a molecular diffusion coefficient (D_m) of 2.08×10^{-9} m/s^2, representative of a dilute bromide tracer. The corresponding Schmidt number ($\mathrm{Sc} = \frac{\mu}{\rho D_m}$) is 428. For solute transport simulations (based on converged steady-state flow solution), we imposed a pulse-type constant concentration at the inlet of the column for 2.78 s then kept it as zero for the rest of the simulation period.

3. Numerical model descriptions

In the current study, we intercompare four major pore-scale numerical approaches that can be divided into two classes: 1) those that explicitly model the three-dimensional geometry of pore spaces and 2) those that conceptualize the pore space as a topologically consistent set of stylized pore bodies and pore throats. Three of the four approaches (FVM-based CFD, LBM, and SPH) belong to class 1, and the fourth (PNM) belongs to class 2. An overview of the five computational codes considered, which implement these four model types, is shown in Table 2, including the model names, institution names, numerical methods used to solve the governing equations for both the flow and transport processes and the class that each pore-scale model belongs to.

Computational meshes used to represent the complex pore geometry for the class 1 simulations were generated in two ways (Fig. 2): 1) Cartesian (structured or unstructured) mesh, and 2) body-fitted

Table 2
Summary of the numerical models.

Name of the code	Institution	Numerical method	Class
TETHYS	PNNL	FVM	1
STAR-CCM+	CD-adapco	FVM	1
iRMB-LBM	TU Braunschweig	LBM	1
ISPH	SNL	SPH	1
UT-PNM	Univ. of Texas at Austin	PNM	2

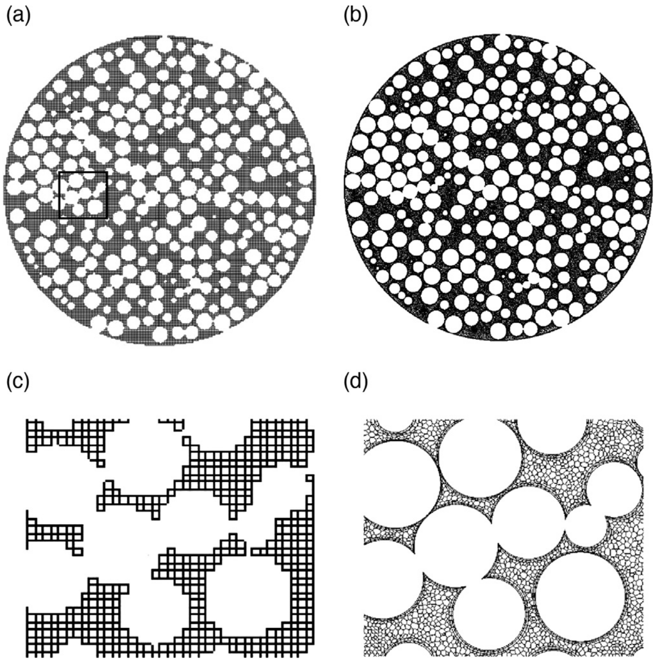

Fig. 2. Representative mesh used in the pore-scale simulations (sampled at a selected slice located at the center of the sphere pack): a) 40 μm-structured (Cartesian) mesh used in CFD-TETHYS; b) unstructured body-fitted mesh used in STAR-CCM+; c) and d) are zoomed-in mesh samples from the same location on the selected slice (indicated by a box in a).

meshes based on the sphere geometry. The direct voxel meshing approach simply used structured Cartesian-type mesh elements defined in direct correspondence to the cubic voxel elements output images from the MRV measurement. The LBM grids were generated using a cut-cell approach taking into account the explicit sphere geometries leading to a second-order accurate geometric description. Two mesh resolutions were used in [30]: 20 μm and 40 μm. The pore geometry was defined from magnetic resonance imaging (MRI) data with a resolution of 20 μm. The MRV experiment was conducted to measure the velocity field at 40 μm resolution. The same mesh resolutions were used directly in the TETHYS (CFD-FVM), iRMB-LBM and ISPH simulations. The STAR-CCM+ code was employed to perform CFD (standard FVM) simulations based on an unstructured body-fitted mesh (40 μm as base size) as described in [30]. UT-PNM used a topologically equivalent but geometrically simplified representation of the pore space as the computational domain (described in Section 3.4).

3.1. FVM-based computational fluid dynamics (CFD)

CFD applications to pore-scale simulations are often referred as direct numerical simulations (DNS, class 1) because the governing conservation equations (mass and momentum) for laminar flow and the passive scalar equation for transport are solved on a fixed mesh that retains the full pore geometry to the limits of the grid resolution and, for grid-independent solutions, are effectively exact solutions of the Navier–Stokes equations. However, the numerical schemes used to solve the governing equations are not the same in different codes. For the current benchmark problem, two different computational codes/packages were tested in this category using standard FVM.

3.1.1. TETHYS

The Transient Energy Transport Hydrodynamics Simulator (TETHYS) code, developed at Pacific Northwest National Laboratory, is a CFD toolkit for environmental simulations with the capabilities to simulate hydrodynamics, solute transport and reactions. TETHYS uses a finite-volume scheme [44] to discretize the governing equations for conversation of mass, momentum (Navier–Stokes equations) and transported scalars on both structured and unstructured meshes. Previous research using TETHYS includes laminar flow and scalar transport in a tube with sinusoidal-wavy wall [45], 3D pore-scale flow in a micro-sized monodispersed sphere pack [30] and 3D pore-scale flow and solute transport in a soil column [46].

The governing equations solved in TETHYS are presented in an integral form. The equations for mass and momentum conservation, and scalar transport over a control volume V with boundary $S := \partial V$ are:

$$\frac{\partial}{\partial t}\int_V \rho \, \mathrm{d}V + \int_S \rho \boldsymbol{u} \cdot \hat{\boldsymbol{n}} \, \mathrm{d}S = 0, \tag{1a}$$

$$\frac{\partial}{\partial t}\int_V \rho \boldsymbol{u} \, \mathrm{d}V + \int_S \rho \boldsymbol{u}\boldsymbol{u} \cdot \hat{\boldsymbol{n}} \, \mathrm{d}S = \int_S (\boldsymbol{\tau} - p\mathsf{I}) \cdot \hat{\boldsymbol{n}} \, \mathrm{d}S + \int_V \boldsymbol{f} \mathrm{d}V, \tag{1b}$$

$$\frac{\partial}{\partial t}\int_V \rho \phi \, \mathrm{d}V + \int_S \rho \phi \boldsymbol{u} \cdot \hat{\boldsymbol{n}} \, \mathrm{d}S = \int_S D_\phi \nabla \phi \cdot \hat{\boldsymbol{n}} \, \mathrm{d}S + \int_V q_\phi \, \mathrm{d}V, \tag{1c}$$

where ρ and $\boldsymbol{u}$ are the fluid mass density and velocity, respectively; $\boldsymbol{\tau}$ is the viscous stress tensor; p is the pressure; I is the 3×3 identity matrix; $\hat{\boldsymbol{n}}$ is the unit vector out-normal to the surface element $\mathrm{d}S$; $\boldsymbol{f}$ is a body force; ϕ is a generic scalar quantity; q_ϕ is a source term; and D_ϕ is diffusivity of ϕ.

TETHYS uses the standard finite volume method (FVM) [47] to discretize the governing PDEs into a system of algebraic equations that are solved using iterative linear algebra methods. A segregated solution scheme based on the SIMPLE algorithm [44] is used to solve the flow field [45]. Second-order convection schemes are available for the transport of both momentum and scalars. These are implemented for unstructured meshes using the TVD (Total Variation Diminishing) methods [48]. In this work, central differencing was used for momentum, and MUSCL (Monotonic Upstream-Centered Scheme for Conservation Laws) [49]) for scalar transport. An implicit first-order scheme is used for transport time marching.

Structured rectilinear meshes with two resolutions (20 μm, 72.1 M cells, and 40 μm, 9.1 M cells) were used in TETHYS simulations (sampled mesh in 40 μm-resolution shown in Fig. 2(a) and (c)). For both meshes, a steady hydrodynamic solution was obtained first, and then used as a constant flow field for the transport simulation. For hydrodynamics, the boundary conditions used in the TETHYS simulation followed the experimental setup. A constant mass flow rate was imposed at the inlet and a constant pressure was imposed at the outlet. All solid walls were treated as no-slip wall boundaries. The initial conditions were zero velocity and constant pressure. For the transport simulation, the passive scalar value was initially zero everywhere. The inlet concentration was set equal to 1.0 for 2.798 s and then 0.0 for the rest of the simulation period (50 s).

The steady-state flow simulations were previously finished and obtained from Yang et al. [30]. The solute transport simulations were performed on the Cascade cluster at the Environmental Molecular Sciences Laboratory (EMSL). The transport simulation on the 40 μm mesh used 480 cores for approximately 7 h. For the 20 μm mesh, the simulation used 1600 cores and took approximately 12 h.

TETHYS was also used to compute a macroscopic effective axial dispersion coefficient directly using the method of volume averaging

(MVA) [50–52]. Richmond et al. [45] provides a full description of the implementation of MVA in TETHYS and a simple application as validation. The major modification of MVA introduced in [45] is the addition of a time derivative term to the MVA equations to allow for its application to unsteady flows. The total dispersion tensor is the sum of the effective diffusivity, $\mathbf{D}_{\text{eff}}$, and hydrodynamic dispersion, $\mathbf{D}_{\beta}$:

$$\begin{aligned}\mathbf{D}^* &= \mathbf{D}_{\text{eff}} + \mathbf{D}_{\beta} \\ &= D_m\left(\mathbf{I} + \frac{1}{V}\int_S \boldsymbol{b}\,\hat{\boldsymbol{n}}\,\mathrm{d}S\right) - \frac{1}{V}\int_V \boldsymbol{b}\,(\boldsymbol{u} - \langle\boldsymbol{u}\rangle)\,\mathrm{d}V,\end{aligned} \qquad (2)$$

where V is the control volume, $S := \partial V$ is the area, $\hat{\boldsymbol{n}}$ is the unit vector out-normal to the surface element dS, D_m is the molecular diffusivity, $\langle\boldsymbol{u}\rangle$ is the velocity averaged over the volume V, and the vector field $\boldsymbol{b}$ satisfies the following equation:

$$\frac{\partial \boldsymbol{b}}{\partial t} + \nabla\cdot(\boldsymbol{u}\boldsymbol{b}) - D_m\nabla^2\boldsymbol{b} = (\boldsymbol{u} - \langle\boldsymbol{u}\rangle). \qquad (3)$$

The above equation for the vector field $\boldsymbol{b}$ is rewritten into the integral form of Eq. (1c) for each component and then solved in TETHYS using FVM.

To use the method of MVA, the domain of interest must have a periodic boundary condition in the axial direction. Only the 40 µm mesh was used. The inlet and outlet boundaries were changed to periodic boundaries with the same pressure drop that was produced in the original hydrodynamic simulation. This condition enforces the constraint that the velocity distribution at the outlet face must match that at the inlet face, but because of the buffer regions this has insignificant impact on the results. The original hydrodynamic solution was used as the initial condition. After convergence, the resulting flux was the same as specified in the CFD simulation. The MVA calculations converged very slowly for the Péclet number corresponding to the simulated case, and thus were computationally very expensive. The calculation was performed on PNNL's Institutional Computing (PIC) clusters (Olympus and Constance) using 480 cores and took approximately 5 days to complete.

3.1.2. STAR-CCM+

The commercial software package STAR-CCM+ (CD-adapco, Melville, NY, USA) was used to simulate pore-scale flow and transport in the sphere pack. Previous research [9,30] demonstrated the advantages and accuracy of using STAR-CCM+ for pore-scale modeling in complex pore geometries. Employing a user-defined automatic sphere generation script implemented in STAR-CCM+, a CAD geometry of the sphere pack was constructed. Then during the embedded mesh generation procedure, the surfaces of the spheres and the pore space were smoothly meshed by polyhedral cells and prism layers (Fig. 2(b) and (d)). Seven million polyhedral cells were generated by this approach, which was previously demonstrated to be sufficient based on mesh-independence studies reported in [30].

Three-dimensional Navier–Stokes equations describing incompressible fluid flow and a passive scalar transport equation at the pore scale were discretized using standard FVM techniques [47] and an algebraic multigrid linear solver. The numerical algorithms included a second-order upwind scheme for convection and diffusion terms, an implicit first-order scheme for time marching. The iterative SIMPLE algorithm was also used to couple the velocity and pressure fields. For flow simulation, the convergence criteria for continuity was set at 10^{-6}.

The boundary conditions, initial condition and flow/solute transport conditions were the same as those in TETHYS. Solute transport simulation was conducted based on the steady-state flow solution. The simulations were run in parallel on a DELL workstation T7500 (Intel® Xeon™ CPU, 2.53GHz, 4 processors). The flow field solution was found to converge in about 3000 iterations requiring 15 h. Upon convergence the flow field was fixed during the solute transport simulation. The time step was 0.01 s for the transient passive scalar simulation with 100 inner iterations. The total simulation time was 50 s, which required 45 h of total computing time.

3.2. Lattice Boltzmann method (LBM)

The lattice Boltzmann simulations were performed with the cumulant lattice Boltzmann method [53]. This method uses a finite velocity discretization of the Boltzmann transport equation using 27 discrete velocities based on the tensor product of the velocities $\{-\xi,\ 0,\ \xi\} := \{-1,\ 0,\ 1\}\xi$ in each Cartesian dimension [54,55], where $\xi := \Delta x/\Delta t$ is the speed quantum; and Δx and Δt are grid spacing and time step size, respectively. The lattice Boltzmann equation is written as:

$$f_{ijk}(\boldsymbol{x} + \boldsymbol{\xi}_{ijk}\Delta t,\ t_n + \Delta t) = f_{ijk}(\boldsymbol{x},\ t_n) + \Omega_{ijk}[f_{ijk}(\boldsymbol{x},\ t_n)], \qquad (4)$$

where $f_{ijk}(\boldsymbol{x}, t_n)$ is the discrete velocity distribution function corresponding to the discrete velocity $\boldsymbol{\xi}_{ijk}$ at the Cartesian coordinates $(x, y, z) := \boldsymbol{x}$ and discrete time t_n, and $i,\ j,\ k \in \{-1,\ 0,\ +1\}$. For the *steady* near incompressible flow with a large pressure drop over the flow domain considered here, we have used the so-called *incompressible* lattice Boltzmann (LB) model [56], in which the density ρ is decomposed into its mean ρ_0 and fluctuation $\delta\rho$, *i.e.*, $\rho := \rho_0 + \delta\rho$, with $\rho_0 = 1$, and the coupling between $\delta\rho$ and the flow velocity $\boldsymbol{u}$ is neglected. In addition, ρ_0 can be ignored in the simulations, so that $\delta\rho$ is the conserved quantity, therefore,

$$\delta\rho := \sum_{i,j,k} f_{ijk}. \qquad (5)$$

The collision operator Ω_{ijk} can be carried out in the space of discrete velocities, or of moments [57–59], or of cumulants [53]. In this work the collision is executed in the cumulant space. The cumulants of the distribution function f_{ijk} are obtained by a series expansion of the logarithm of its bilateral Laplace transform $\mathcal{L}$:

$$C_{nrs} := \xi^{-(n+r+s)} \frac{\partial^n\partial^r\partial^s}{\partial\Lambda_x^n\,\partial\Lambda_y^r\,\partial\Lambda_z^s} \ln\left(\mathcal{L}[f_{ijk}(\boldsymbol{\xi}) + w_{ijk}(1 - \delta\rho)]\right)\Big|_{\boldsymbol{\Lambda}=\mathbf{0}}, \qquad (6)$$

where $\boldsymbol{\Lambda} := (\Lambda_x,\ \Lambda_y,\ \Lambda_z)$ is the transform variable of the bilateral Laplace transform, and w_{ijk} are the constant weight coefficients [54,55]:

$$w_{ijk} = \begin{cases} \dfrac{8}{27}, & \|\boldsymbol{\xi}_{ijk}\| = 0, \\ \dfrac{2}{27}, & \|\boldsymbol{\xi}_{ijk}\| = \xi, \\ \dfrac{1}{54}, & \|\boldsymbol{\xi}_{ijk}\| = \sqrt{2}\xi, \\ \dfrac{1}{216}, & \|\boldsymbol{\xi}_{ijk}\| = \sqrt{3}\xi, \end{cases} \qquad (7)$$

which satisfy the normalization condition $\sum_{ijk} w_{ijk} = 1$. Note that the Laplace transform in Eq. (6) is with respect to the molecular velocity $\boldsymbol{\xi}$, thus the term $w_{ijk}(1 - \delta\rho)$ should be treated as a constant one. The reason to replace $\delta\rho$ with 1 in f_{ijk} in Eq. (6) is to automatically generate the correct cumulants corresponding to the incompressible LB model. Here, the cumulants are expressed in terms of the central moments m_{nsr} of f_{ijk} defined by:

$$m_{nrs} = \sum_{ijk} c_{ijk,x}^n c_{ijk,y}^r c_{ijk,z}^s f_{ijk}, \qquad (8)$$

where $c_{ijk,x}$, $c_{ijk,y}$, and $c_{ijk,z}$ are the Cartesian components of the peculiar velocity $\boldsymbol{c}_{ijk} := (\boldsymbol{\xi}_{ijk} - \boldsymbol{u})$. For the compressible LB model with the coupling between ρ and $\boldsymbol{u}$, the central moments of order $2n$ have an $\boldsymbol{u}$-independent term $\rho(\sqrt{\theta})^{2n}$, where $\theta = c_s^2 = 1/3$ and c_s is the speed of sound in the LBE. This term becomes $\rho_0(\sqrt{\theta})^{2n} = \theta^n$ for the incompressible LB model with $\rho_0 = 1$, which is correctly generated by Eq. (6) automatically.

The collisional invariants (or the conserved quantities) in terms of cumulants in the model are:

$$C_{000} := 0,$$
$$(C_{100}, C_{010}, C_{001}) := (u, v, w) := \boldsymbol{u}.$$

In what follows, we will use the conventional notation of permutation, *i.e.*, $(nr\dots s)$, to denote all possible permutations of indices $\{n, r, \dots, s\}$. In addition to the conserved cumulants, the only other cumulants with non-zero equilibria are [53]:

$$C_{(200)}^{(\mathrm{eq})} = \theta = \frac{1}{3}. \tag{9}$$

For the remaining 20 cumulants, their equilibria are zero. When the distribution f_{ijk} is computed from the cumulants $\{C_{nrs}\}$, the mass conservation is reinstalled by requiring that $\sum_{ijk} f_{ijk} = \delta\rho$.

In the collision, cumulants $\{C_{nrs}\}$ are relaxed towards their equilibria $\{C_{nrs}^{(\mathrm{eq})}\}$ with relaxation rates ω_{nrs}:

$$C_{nrs}^{*} = C_{nrs} - \omega_{nrs}\cdot\left(C_{nrs} - C_{nrs}^{(\mathrm{eq})}\right), \tag{10}$$

where the superscript $*$ denote the post-collision state. The kinematic viscosity ν is determined by the relaxation rates for the second-order cumulants $C_{(110)}$, $(C_{200} - C_{020})$, and $(C_{200} - C_{002})$ [53]:

$$\nu = \frac{1}{3}\left(\frac{1}{\omega_{110}} - \frac{1}{2}\right)\xi^2\Delta t, \tag{11}$$

and the bulk viscosity is $\zeta = (1/6)\xi^2\Delta t$ with the choice of the relaxation rates.

We noted that the relaxation rates for the third-order cumulants $C_{(120)}$ affect the value of computed permeability [60]. We used the following value in this work:

$$\omega_{120} = \frac{8(2-\omega_{110})}{8-\omega_{110}}. \tag{12}$$

Coupling the relaxation rate of the third-order cumulants $C_{(120)}$ to that of the second-order cumulant $C_{(110)}$ eliminates the spurious dependence of the permeability on the viscosity ν encountered in lattice Boltzmann methods using the collision operator with one relaxation rate [60]. The relaxation rates for the remaining cumulants are all set to unity. It has been shown that the cumulant lattice Boltzmann method solves the incompressible Navier–Stokes equations for $\delta\rho$ and $\boldsymbol{u}$ in the limit of small Mach and Knudsen numbers [53].

For scalar transport, an advection diffusion equation is solved using the same discretization and the same hardware as for the flow solver with 27 discrete velocities. The advection velocity in the scalar transport is the steady velocity field $\boldsymbol{u}(\boldsymbol{x})$ obtained from the lattice Boltzmann flow solver on the same mesh. The advection-diffusion lattice Boltzmann equation reads:

$$h_{ijk}(\boldsymbol{x} + \boldsymbol{\xi}_{ijk}\Delta t,\, t_n + \Delta t) = h_{ijk}(\boldsymbol{x},\, t_n) + \Omega_{ijk}[h_{ijk}(\boldsymbol{x},\, t_n)]. \tag{13}$$

The collision operator Ω_{ijk} in Eq. (13) is carried out in central moment space, *i.e.*, the moments of the peculiar velocity $\boldsymbol{c}_{ijk} := (\boldsymbol{\xi}_{ijk} - \boldsymbol{u})$. The central moments are computed from the shifted Laplace-transform of the distribution function h_{ijk} with a given flow velocity $\boldsymbol{u} := (u, v, w)$:

$$m_{nrs} = \xi^{-(n+r+s)} \frac{\partial^n\partial^r\partial^s}{\partial\Lambda_x^n\partial\Lambda_y^r\partial\Lambda_z^s} e^{-\boldsymbol{u}\cdot\boldsymbol{\Lambda}}\mathcal{L}[h_{ijk}(\boldsymbol{\xi})]\Big|_{\boldsymbol{\Lambda}=\boldsymbol{0}}. \tag{14}$$

Note that the above equation is equivalent to Eq. (8) for f_{ijk}.

The collision is carried out with the central moments orthogonalized by the following linearized factorization:

$$M_{(100)} = m_{(100)}, \tag{15a}$$

$$M_{(110)} = m_{(110)}, \tag{15b}$$

$$M_{111} = m_{111}, \tag{15c}$$

$$M_{(200)} = m_{(200)} - \frac{1}{3}m_{000}, \tag{15d}$$

$$M_{(210)} = m_{(210)} - \frac{1}{3}m_{(010)}, \tag{15e}$$

$$M_{(220)} = m_{(220)} - \frac{1}{9}m_{000}, \tag{15f}$$

$$M_{(221)} = m_{(221)} - \frac{1}{9}m_{(001)}, \tag{15g}$$

$$M_{222} = m_{222} - \frac{1}{27}m_{000}. \tag{15h}$$

The only conserved central moment is $m_{000} = \delta\rho$, *i.e.*, the mass density. The equilibria of all other factorized central moments M_{nrs} are zero. Therefore, the collision process is realized by the following relaxation:

$$M_{nrs}^{*} = (1 - \omega_{nrs})M_{nrs}. \tag{16}$$

The diffusivity D is determined only by the relaxation rates of $m_{(100)}$:

$$D = \frac{1}{3}\left(\frac{1}{\omega_{100}} - \frac{1}{2}\right)\xi^2\Delta t. \tag{17}$$

All the other relaxation rates are set to unity.

The no-slip boundary conditions (BCs) are realized by the bounce-back (BB) scheme [35,61,62]. The curved boundaries of the spheres are approximated by their intersections with all 26 links from one grid point to its neighboring grid points defined by the discrete velocities $\{\boldsymbol{\xi}_{ijk}\}$, and the missing distributions f_{ijk} needed for the BB-BCs at the curved boundaries are obtained through interpolations [35,53,61,62]. The interpolations ensure that the accuracy of the boundary conditions is consistent with that of the lattice Boltzmann flow solver [53]. Thus the complex geometry of the porous medium is accurately represented in the LBM, and the representation of the curved boundaries accurately approximates the body-fitted mesh shown in Fig. 2(d). Specifically, the interpolations used here to treat curved boundaries are [53]:

$$f_{\overline{ijk}}(\boldsymbol{x},\, t_n + \Delta t) = \frac{1}{1+q}\Big[q\Big(f_{ijk}^{*}(\boldsymbol{x},\, t_n) + f_{\overline{ijk}}^{*}(\boldsymbol{x},\, t_n)\Big) + (1-q)f_{ijk}(\boldsymbol{x},\, t_n)\Big], \tag{18}$$

where $f_{\overline{ijk}} := f(\boldsymbol{\xi}_{\overline{ijk}})$, $\boldsymbol{\xi}_{\overline{ijk}} := -\boldsymbol{\xi}_{ijk}$, and $0 \le q < 1$ is the portion of a link $\|\boldsymbol{\xi}_{ijk}\|\Delta t$ inside the fluid region [61]. Other boundary conditions are the Dirichlet one for the velocity at the inlet, and non-reflective extrapolation at the outlet [53]. More details about implementing the boundary conditions are given by Geier et al. [53].

The incompressible cumulant lattice Boltzmann method is implemented for parallel execution on General Purpose Graphics Processing Units (GPGPUs) with Compute Unified Device Architecture (CUDA). The geometry was discretized with a sparse Cartesian grid using the Eso-Twist data structure [63]. The communication between GPGPUs was done using MPI. Two grid resolutions are considered. The grid with a resolution of 20 μm has about 53.5 million nodes, while the grid with resolution of 40 μm has about 6.7 million nodes. The simulation with the lower resolution mesh running on a single TESLA® K40c GPGPU took about 4.5 h for the flow simulation of about 72 s in real time. We have achieved a performance of approximately 233.3 million node updates per second (MNUPS). The simulation with the higher resolution mesh was distributed over two TESLA® K40c GPGPUs and took about 61.07 h for the flow simulation of about 72 s in real time.

3.3. Smoothed Particle Hydrodynamics (SPH)

In this work we use a consistent second-order Incompressible Smoothed Particle Hydrodynamics (ISPH) method [64]. The method is implemented using the massively parallel particle library LAMMPS [65] and the linear algebra library Trilinos [66]. LAMMPS is used to provide a computational framework for large-scale particle-based simulations, *e.g.*, domain decomposition, load balancing, (re)neighboring of particles, communication of particle-associated data fields, *etc.* To provide an implicit time-integration capability, the Trilinos solver packages are used, *i.e.*, Epetra [67] for distributed linear algebra, Belos [68] for a GMRES solver, and ML [69] for an algebraic multigrid preconditioner.

The smoothed particle hydrodynamics (SPH) method is a fully Lagrangian particle method for solving conservation equations. Traditionally, incompressible fluids are treated in SPH as weakly compressible fluids and an equation of state is used to close the system of the momentum and continuity equations. The speed of sound, c is chosen so that the Mach number Ma satisfies the condition $\mathrm{Ma} = \frac{v}{c} \leqslant 0.1$. Under this condition, the compressible fluid behaves as incompressible. Standard SPH discretization is based on the bell-shaped compactly-supported kernel $W(x)$, and represents spatial derivatives of any function in terms of the values of this function at discretization points and derivatives of W. The advantage of standard SPH is that the resulting momentum equations have the form of the equations of Molecular Dynamics, *i.e.*, the SPH discretization of the continuity, momentum, and advection diffusion equations exactly conserves mass and momentum and, when explicit time integration is used, the SPH algorithms are easily parallelizable. There are two main challenges in application of the weakly-compressible time explicit SPH method to flow in porous media. The accuracy of the standard SPH discretization is hard to control as it depends on the SPH particle distribution. As particles become disordered, the convergence rate of SPH method becomes less than two with respect to the resolution parameter, h, the support of W. The second challenge is that the time step in explicit time integration schemes, subject to the CFL conditions (Courant–Friedrichs–Lewy condition, [70]), becomes prohibitively small because of the speed of sound and viscosity constraints. A review of the SPH methods with application to pore-scale flows can be found in [40].

The consistent ISPH method uses an incremental pressure correction scheme to ensure divergence-free velocity fields, which relaxes CFL constraints and allows taking significantly larger time steps comparing to those used in the weakly compressible SPH. To achieve second-order accuracy in time and space, the ISPH method uses the Crank–Nicholson scheme for time discretization and corrected differential operators for the space discretization. The use of the corrected operators allows for smaller support h than that needed by the standard SPH method.

ISPH simulations with two different resolutions were performed. In these simulations, SPH particles were initially placed on Body-Centered Cubic (BCC) lattice with grid sizes 40 μm and 20 μm. SPH particles located inside the spheres were labeled as solid particles.

Application of the Takeda/Morris no-slip boundary condition requires the evaluation of the perpendicular distances to walls for fluid particles interacting with dummy particles. In increasingly complex boundary configurations this becomes cumbersome and in general requires some sort of piecewise spline representation of the boundaries. To circumvent this we have implemented the smoothed perpendicular distance approximation introduced by Holmes et al. [71].

Solid particle positions are fixed in space and used to impose the Morris no-slip boundary condition [72] using area coordinates described in [71]. The rest of the particles are labeled as fluid particles, and their positions are advected in time with velocities found from the ISPH solution of the Navier–Stokes equations. We prescribed periodic boundary conditions at the top and bottom of the sphere pack and the flow is driven by a body force mimicking the constant pressure drop predicted by Darcy's law. Periodic boundary conditions are more natural for Lagrangian methods. The presence of the two buffer regions makes the solution in the sphere pack essentially unaffected by this particular choice of boundary conditions. The initial velocity is set to zero and the N–S equations are integrated with variable time step sizes (in each time iteration, a timestep size is adjusted with respect to the maximum velocity of fluid particles) until steady state average velocity was reached.

Table 3
Summary of the mesh, grid size and run time.

Code	Mesh type	Grid size	Cell No.	Machine	Run time[a]	
TETHYS	Cartesian	20 μm	72.1M	1600 CPUs	9 h 12 h	(f, ss) (t, ts)
TETHYS	Cartesian	40 μm	9.1M	480 CPUs	4 h 7 h	(f, ss) (t, ts)
iRMB-LBM	Cartesian	20 μm	53.5M	2 TESLA K40c	61.07 h 25.33 h	(f, ts) (t, ts)
iRMB-LBM	Cartesian	40 μm	6.7M	1 TESLA K40c	4.5 h 1.5 h	(f, ts) (t, ts)
ISPH	Meshless	20 μm	165M	7680 CPUs	13 min	(f, ts)
ISPH	Meshless	40 μm	25M	960 CPUs	10 min	(f, ts)
STAR-CCM+	Polyhedral	40 μm	13M	4 CPUs	15 h 45 h	(f, ss) (t, ts)
UT-PNM	–	–	–	Single CPU	1 s 45 s	(f, ss) (t, ts)

[a] (f: flow simulation; t: solute transport; ss: steady-state simulation; ts: transient simulation).

The simulations were run on the Edison supercomputer, Cray® XC30, at the National Energy Research Scientific Computing (NERSC) center. A compute node consists of two sockets each of which has a 12-core Intel® Ivy Bridge 2.4 GHz processor and compute nodes are connected via the Cray Aries interconnect. Table 3 shows weakly scalable results; the largest problem for 20 μm takes less than 15 min to reach the steady-state solution.

3.4. Pore-network model (PNM)

The University of Texas at Austin (UT-Austin) group used a pore-network model (PNM) to simulate flow and transport through the column. Pore networks are simplified representations of the complicated pore space geometry with a topologically-equivalent network of interconnected elements: pores and throats. Pores represent locally larger void spaces that are connected via narrower constrictions or throats. Pores and throats are typically assigned simple shapes (*e.g.*, spheres and cylinders, respectively) that make them amenable to analytic expressions for flow and transport. The flow equation is obtained by imposing mass balance at every pore and since the fluid is Newtonian and incompressible, this results in a linear system of equations. Solving this system yields the pressure and velocity fields needed for subsequent solution of the transport equation. The details are explained in [73].

Three PNM models were considered for the simulation of transport: a) the mixed-cell method (MCM) (*e.g.*, [74,75]), b) the streamline-splitting method (SSM) [42], and c) the superposing transport method (STM) [73,76]. All models are Eulerian or grid-based (no particles are tracked). MCM is the simplest and more commonly used of the three. In it, solute balance is imposed on each pore, resulting in a linear system of ODEs for pore concentrations. In MCM, all the void volumes are assigned to the pores, throats are assumed to be volumeless, solute is perfectly mixed within the pores, and the shearing of solute due to non-uniform velocity profiles within throats (hereafter referred to as "shear dispersion") is ignored. It is therefore computationally very efficient. SSM is similar to MCM in all respects except that it accounts for the partial mixing of solute within pores. On the other hand, STM differs from MCM in that throats assume a portion (a user defined quantity) of the void volume, and shear-dispersion within throats is included in the modeling. Mehmani and Balhoff [76] showed that SSM and MCM produce practically identical results in disordered sphere packs, entailing that mixing assumptions within pores have seemingly negligible impact on longitudinal macroscopic dispersion in these media. Similarly, they showed that STM and MCM predictions are very close for the Péclet numbers considered in this work ($\mathrm{Pe} := \mathrm{Re}_p \times \mathrm{Sc} = 257$). Additional tests on the sphere pack considered herein confirmed these conclusions. We therefore only present the MCM results in this work. Further details of the transport models are omitted for brevity and can be found in the references given.

For compatibility reasons with the UT-PNM codes used herein, the cylindrical sphere pack column was cropped into a cuboid with the same length in the *y*-direction, and a square-shaped cross-section with a diagonal distance equal to the cross-sectional diameter of the cylindrical column. The pore-network was extracted from the cropped domain using LSU's Avizo module, which employs techniques outlined in [77]. Briefly, a maximal ball algorithm is used to locate the centers of each pore. Throat hydraulic conductivities are then calculated using methods from [78], whereby irregular throat shapes are mapped onto triangular, square, and circular geometries, depending on their shape factors. A constant pressure gradient was imposed on the pore network in the *y*-direction to establish steady-state flow and compute the pressure/velocity fields. Solute was then injected through the inlet by imposing a constant inlet concentration of 1 for the duration of 2.798 s, which was thereafter set to 0 for the rest of the simulation. Zero concentration gradient was imposed at the outlet. Breakthrough curves were obtained by computing the flux-averaged concentrations of all throats at the outlet face of the network.

All simulations were run in series on a single desktop machine with an Intel® Core™ i7-4790 CPU with a 3.6 GHz processor and 32 GB of Random Access Memory. The implementation of MCM is in MATLAB® and makes effective use of vectorization and avoidance of explicit loops. The transport equation is solved using the adaptive time stepping `ode23tb` solver in MATLAB®, which is an implementation of TR-BDF2, and the implicit Runge–Kutta formula. The wall-clock times for solving the flow and transport equations for the entire duration of the simulation (*i.e.*, 40 simulation seconds or 2.5 pore volumes injected) are 1 and 45 s, respectively.

3.5. Summary of the numerical models

A total of four pore-scale models (five computational codes/packages), belonging to two classes of approaches, were used to simulate flow and transport in the benchmark sphere pack problem. As described in the previous sections, the geometries of the computational domain, the flow/solute transport conditions and the boundary/initial conditions were the same for class 1 models; while the class 2 model UT-PNM used a slightly different setup as explained in Section 3.4. In order to accommodate code differences while maintaining consistency, different specific treatments have been applied. For TETHYS, STAR-CCM+ and iRMB-LBM simulations, constant velocities were applied at the inlet to match the volumetric flow rate used in the MRV experiment. However, in ISPH simulations, a gravitational body force was calculated using the computed pressure drop between the inlet and outlet and then applied to the computational domain in order to match the same Reynolds number. UT-PNM imposed a constant pressure gradient on the pore network in the flow direction to achieve the same Reynolds number as used in the other models. In all the models, no-slip boundary conditions have been used on the other solid surfaces including the surfaces of the spheres and the bounding cylindrical walls. For each code, we conducted flow rate checks to insure mass balance and consistency; the discrepancies in flow rate are all less than 5%.

For the mesh and performance review, a summary is given in Table 3, which includes the name of the code, the mesh used in the simulation (mesh type, grid size and number of cells) and computing cost. It is obvious that UT-PNM runs the fastest due to the relative simplicity of the model. On the other hand, the computational costs of the DNS were substantial, with run times up to several days on supercomputers to solve flow equations on the large mesh needed to fully resolve the complex pore geometry. With the implementation of the modern GPGPU technique (CUDA), the computing time was significantly reduced in the iRMB-LBM runs (transient simulations for both flow and solute transport simulations while TETHYS and STAR-CCM+ ran steady-state simulations for flow). Although the methods do not impose inherent limitations on transport simulation, ISPH did not participate in the solute transport simulations due to specific limitations of the code capabilities and high computing costs.

4. Results

In this section, we present a series of comparisons of flow and transport simulation results among the five considered pore-scale codes/packages. First, several attributes of the simulated velocity fields are evaluated including macroscopic pressure drop and permeability, contour plots of velocities, point-by-point velocity values at selected locations and velocity distributions (histograms). Second, for the transport simulations, breakthrough curves are presented followed by analyses of effective dispersion using both analytical solution fitting and a volume averaging method.

4.1. Flow field

4.1.1. Pressure drop and permeability

The pressure drop across the sphere pack column is an important measure of the macroscopic performance of the pore-scale models. The intercomparisons consider the average pressure difference between the inlet and outlet of the column. For each simulation, the values of the pressure were averaged over the inlet and outlet faces after the flow field reached steady state (UT-PNM solves the steady-state flow equation directly). As verified by numerical tests, the buffer regions had negligible impact on the simulated values of the pressure drop since there was no porous medium to impede flow in the buffer zones. For reference, the expected pressure drop across the uniform sphere pack is 14.29 Pa as estimated through correlations presented in [79,80] and 13.19 Pa using the well-known Carman–Kozeny equation [81]. The simulated values of the pressure drop are summarized in Table 4. Using a structured voxel mesh, the simulated pressure drops from TETHYS simulations are 13.32 Pa (40 μm grid) and 13.19 Pa (20 μm grid), with a difference of less than 1% between the two grid resolutions. Using the same grid resolutions and the cut-cell approach, the pressure drops from iRMB-LBM simulations are 15.24 Pa and 16.07 Pa, which are higher than those computed from TETHYS. The particle resolutions used in the ISPH simulations are the same as those in TETHYS simulations and result in very similar calculated pressure drops of 13.63 Pa and 13.72 Pa, respectively. Also giving

Table 4
Comparison of the pressure drop (ΔP) along the axial direction of the sphere pack.

Numerical method	ΔP (Pa)	Permeability cm^2
[Eisfeld, Reichelt]	14.29	3.93×10^{-6}
Carman-Kozeny Eq.	13.19	4.25×10^{-6}
TETHYS (40 μm)	13.32	4.21×10^{-6}
TETHYS (20 μm)	13.19	4.25×10^{-6}
iRMB-LBM (40 μm)	15.24	3.68×10^{-6}
iRMB-LBM (20 μm)	16.07	3.49×10^{-6}
ISPH (40 μm)	13.63	4.11×10^{-6}
ISPH (20 μ m)	13.72	4.08×10^{-6}
STAR-CCM+	13.65	4.11×10^{-6}
UT-PNM	13.26	4.23×10^{-6}

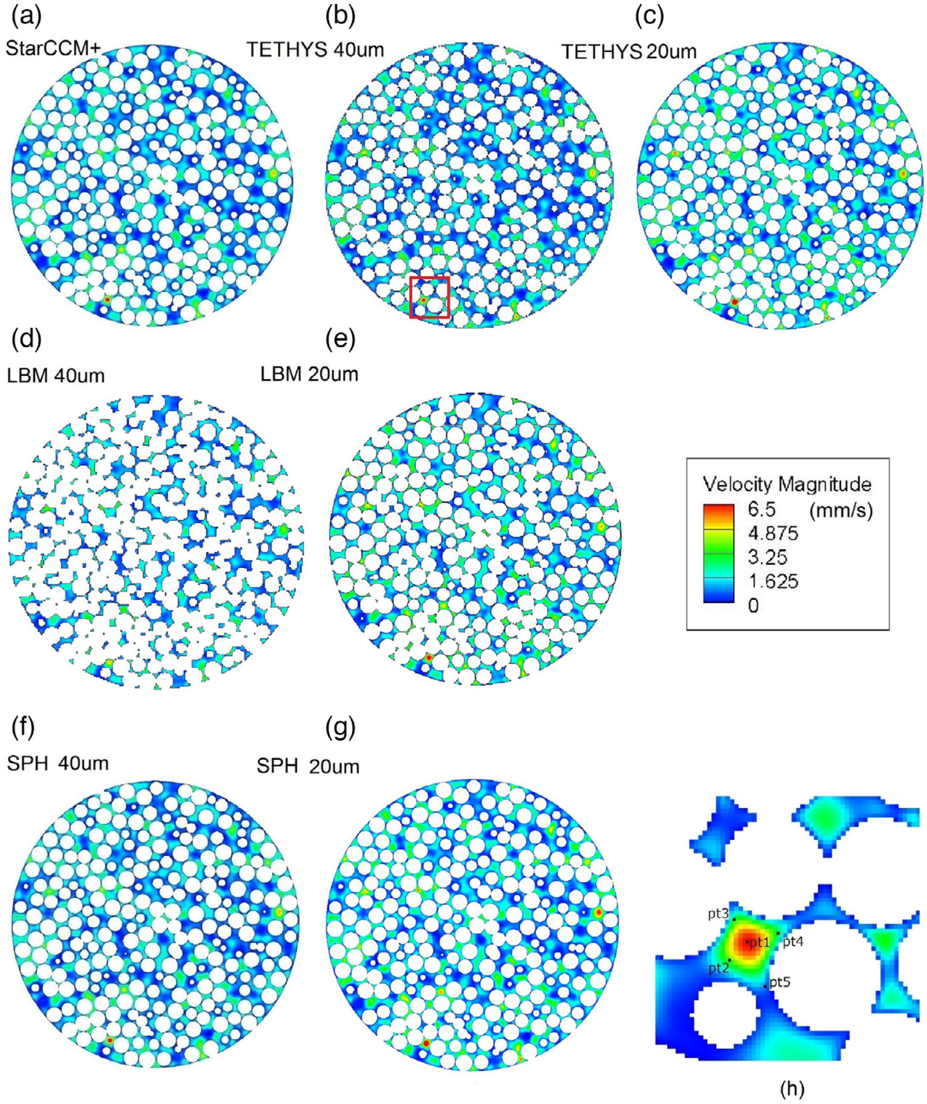

Fig. 3. Color contour plots of velocity in slice 320 (in the middle of the packed-bed at $y = 6.4$ mm): (a) STAR-CCM+ simulation; (b) TETHYS 40 μm simulation; (c) TETHYS 20 μm simulation; (d) iRMB-LBM 40 μm simulation; (e) iRMB-LBM 20 μm simulation; (f) ISPH 40 μm simulation; (g) ISPH 20 μm simulation; (h) magnified visualization of velocity fields in the subregion of slice 320 indicated by a red frame in (b).

very similar results for the simulated pressure drop at 13.65 Pa was the STAR-CCM+ code (using an unstructured body-fitted mesh). The voxel meshes approximate the smooth surfaces of the micro-spheres in a stair-step manner, which not only lead to differences between the porosity of the model system and that measured by the MRI experiments, but may also lead to artifacts in the computed flow field, particularly at relatively coarse grid resolutions. For the class 2 model UT-PNM, although the computational domain was modestly cropped to accommodate code constraints, the simulated pressure drop along the sphere pack is 13.26 Pa, which is very similar to results of several of the other codes.

Given the total flux and pressure drop, the permeability associated with each simulation can also be calculated. The results are also listed in Table 4. The calculated permeabilities of the packed bed, based on the simulated pressure drop for the class 1 models, are around 4.1×10^{-6} cm^2. The corresponding estimate from the class 2 model (UT-PNM) is 4.23×10^{-6} cm^2, very close to the value simulated by the class 1 approaches. This value is in the typical range observed for clean well-sorted sand. Therefore the simulated macroscopic behavior is consistent with that expected based on established empirical relationships for packed bed systems.

4.1.2. Pore-scale velocity comparisons

Contour plots of the simulated velocity magnitude along a selected axial slice ($y = 6.4$ mm) in the middle of the sphere pack, obtained from all class 1 pore-scale models, are shown in Fig. 3. This slice has been chosen as a representative to show the characteristics of the velocity field in the pore space. We find similar flow field patterns in the pore space simulated using different models with either structured mesh (TETHYS), Cartesian mesh with cut-cell approach (iRMB-LBM), body-fitted mesh (STAR-CCM+), or meshless particles (ISPH). However, the magnitudes of the velocities are not identical. We also note that higher velocities are observed in the near-wall region, where the local porosity is higher than average because of the effect of the wall on the arrangement of nearby grains. Differences among the local velocity values computed by the various models can be seen more clearly in detailed views. Fig. 3h shows an expanded view of the subregion of slice 320 indicated by the red box in Fig. 3b. Five locations in this subregion (around a pore with high velocity) were selected to compare point-to-point values. Table 5 provides a tabular listing of the actual values of three velocity components (axial and two transverse directions) at all five points. We note that the values predicted by class 1 models are mostly similar, but in selected

Table 5
Comparison simulated values of axial and transverse velocity components at five selected locations in slice 320 indicated in Fig. 3(h).

	STAR-CCM+	TETHYS		LBM		ISPH	
		20 μm	40 μm	20 μm	40 μm	20 μm	40 μm
	v_y (mm/s)						
Point 1	7.142	7.038	6.622	7.261	5.288	6.847	6.035
Point 2	5.387	5.942	5.667	6.487	4.921	5.323	5.453
Point 3	5.186	5.013	4.774	4.034	2.788	5.191	5.213
Point 4	1.860	2.042	1.958	2.358	1.497	1.862	1.890
Point 5	0.425	0.431	0.407	1.298	1.100	0.424	0.432
	v_x (mm/s)						
Point 1	−0.550	−0.566	−0.584	−0.629	−0.447	−0.541	−0.562
Point 2	−0.542	−0.539	−0.514	−0.684	−0.505	−0.539	−0.548
Point 3	−0.636	−0.641	−0.622	−0.706	−0.424	−0.635	−0.642
Point 4	−0.096	−0.094	−0.102	−0.082	−0.059	−0.089	−0.092
Point 5	0.088	0.093	0.090	0.091	0.025	0.086	0.084
	v_z (mm/s)						
Point 1	−1.824	−1.852	−1.773	−1.975	−1.430	−1.814	−1.791
Point 2	−1.484	−1.430	−1.391	−1.624	−1.213	−1.464	−1.452
Point 3	−0.974	−1.103	−1.102	−1.116	−0.849	−0.945	−0.958
Point 4	−0.942	−0.931	−0.906	−0.683	−0.443	−0.941	−0.947
Point 5	−0.634	−0.592	−0.682	−0.858	−0.604	−0.641	−0.659

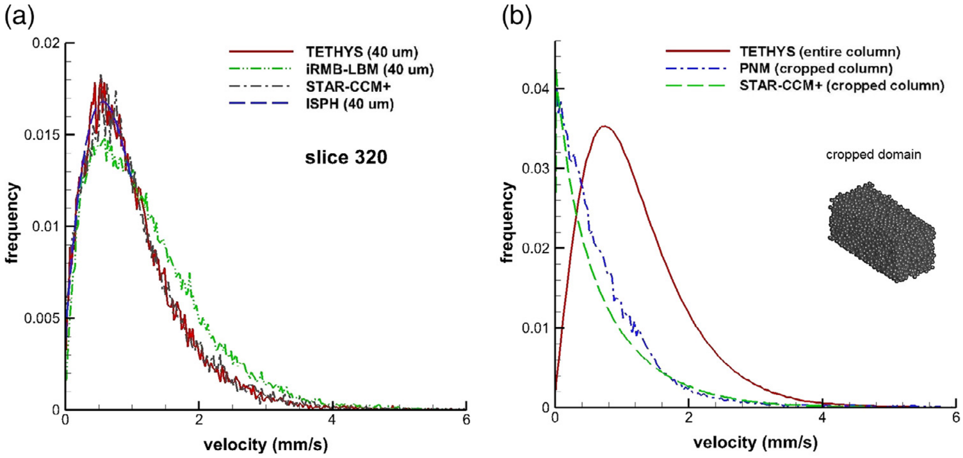

Fig. 4. Comparisons of local velocity histograms: a) among class 1 models for results in a single slice extracted from the center of the column; and b) between STAR-CCM+ (class 1) and UT-PNM (class 2) models for results in the cropped domain.

cases the differences are significant, in particular in those models that employed different grid resolutions or mesh types. For global measurements of the simulated velocity fields, comparisons of velocity histogram in slice 320 (using 300 bins) are shown in Fig. 4a. The conclusions are consistent with the comparisons of the velocity contour plots and point-to-point values.

Since the class 2 model UT-PNM uses a geometrically simplified pore structure, it is not feasible to directly compare local flow velocities with other models. However, a histogram plot of average velocities in the pore throats is useful for comparison purposes. Due to constraints of the UT-PNM code, the sphere pack was cropped into a box-shaped domain (shown in Fig. 4b) with a rectangular cross-section as explained in Section 3.4. For consistency of comparison, a single run using a class 1 model, *i.e.*, STAR-CCM+, was conducted to simulate flow and solute transport in the same cropped domain. Fig. 4b shows the histogram plots of simulated flow fields for the cropped domain using STAR-CCM+ and UT-PNM. The histogram plot for the entire cylindrical column simulated by TETHYS [30] is also shown for reference. It is clear that most of the velocities are in the range from 0 to 2 mm/s for the cropped domain simulations. The velocity distribution in the cropped domain is significantly different from that in full column simulation but for the same cropped domain, the distributions of the velocities computed by STAR-CCM+ and UT-PNM were very similar, demonstrating that PNM accurately represents the pore-scale velocity distribution in a complex pore geometry. The significant differences between the cropped and full domains are associated with high-velocity flows caused by differences in grain packing near the column walls, as illustrated in Fig. 5.

4.2. Solute transport

4.2.1. Breakthrough curves

In this section, computed results for solute transport are presented and compared between class 1 and 2 simulations. Fig. 5 shows three-dimensional visualizations of tracer concentration in the sphere pack at four selected times ($t = 5$, 15, 25, and 35 s), which were simulated by TETHYS (class 1 CFD-FVM). Since a pulse-type constant concentration was imposed at the inlet, the highest concentrations occur in the early stages of the transport simulation (Fig. 5(a)). From those images, it is clear that the pore geometry has a major impact on the character of the transport simulation. It is evident that there is strong preferential flow along the column walls, which is an artifact that would not occur in the natural system. In the absence of this wall effect, the porosity and effective hydraulic conductivity

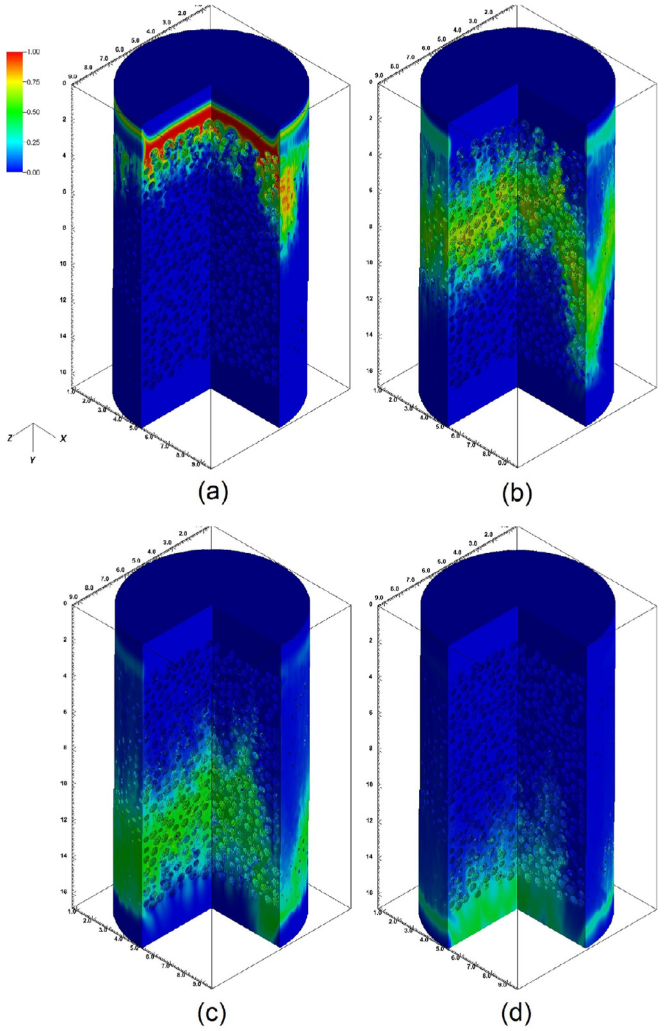

Fig. 5. Visualizations of tracer concentration at four selected simulation times simulated by TETHYS: (a) 5 s; (b) 15 s; (c) 25 s; (d) 35 s.

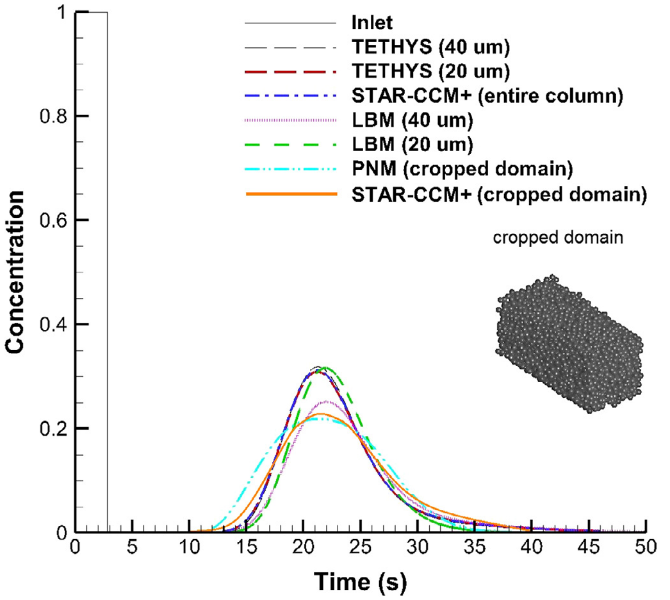

Fig. 7. Computed breakthrough curves (concentration of solute tracer over time) at the outlet of the column versus the pulse-type incoming concentration.

would be smaller, and (given the same Darcy flux) the tracer breakthrough would occur earlier.

Fig. 6 shows the contour plots of the solute concentrations on three selected slices ($y = 4.4$ mm, 6.4 mm, 8.4 mm, respectively) at time = 10 s, as simulated by the TETHYS code. The locations of the selected slices are toward the inlet, in the middle and toward the outlet of the domain. Fig. 6(a) indicates that the highest tracer concentrations are closer to the inlet of the domain where the pulse was imposed. It is clear from Fig. 6(b) and (c) (and also Fig. 5) that preferential flow paths exist along the column wall; solute that travels through the middle of the column moves more slowly. This behavior of the solute could potentially lead to extended tailing in the corresponding breakthrough curve. However, examination of the breakthrough tails in logarithmic plots (not shown) indicates close to log-linear behavior (no anomalous tailing), at least for the period simulated (normalized breakthrough concentrations approaching 0.001).

Fig. 7 shows simulated breakthrough curves at the outlet of the sphere pack column for the bromide tracer. Four pore-scale models from both class 1 (TETHYS, STAR-CCM+, iRMB-LBM) and class 2 (UT-PNM) approaches were used to simulate solute transport based on the flow field solutions. As noted previously, ISPH was not included in the transport comparison due to code limitations. At the inlet, we employed a pulse-type incoming concentration (duration = 2.78 s, 0.1 pore volume) as denoted in the figure. At the outlet, breakthrough concentrations were calculated from the simulation results using a flux-weighted average at each time step. The breakthrough curve results are consistent with the interpretations drawn from the visualizations (Fig. 5). The peak of the breakthrough curves occurs at around 21 s, which includes the time for the solute traveling through the extruded buffer regions added to the sphere pack. The breakthrough curves computed from TETHYS using both 40 μm and 20 μm structured mesh are very similar to each other and to the results from STAR-CCM+ using the unstructured body-fitted mesh.

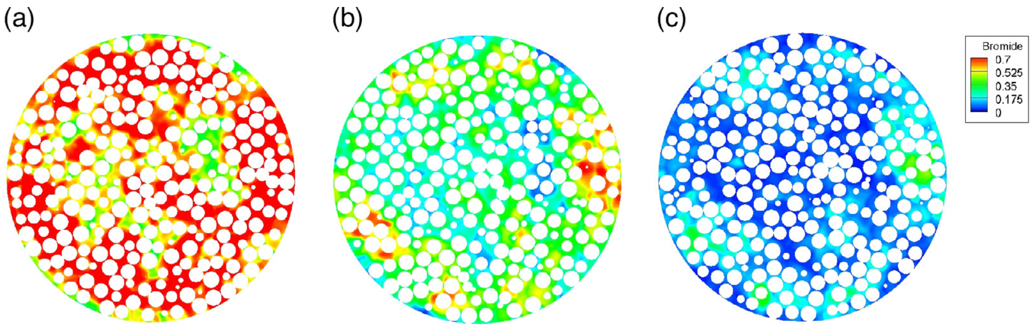

Fig. 6. (a) Contour plot of simulated (TETHYS) tracer concentration at time = 10 s in slice at $y = 4.4$ mm; (b) Contour plot of tracer concentration at time = 10 s in slice at $y = 6.4$ mm; (c) Contour plot of tracer concentration at time = 10 s in slice at $y = 8.4$ mm.

The iRMB-LBM tracer simulation based on the 40 μm-unstructured mesh (using the cut-cell approach) underestimated the maximum solute concentration in the column, while using 20 μm-resolution led to results much closer to the other models, although the peak arrival in the iRMB-LBM simulations was slightly delayed relative to the other models. Despite these minor differences, all the class 1 models demonstrated similar solute breakthrough behavior. However, the breakthrough curve simulated using the class 2 model UT-PNM differs significantly from those of the class 1 models. Since UT-PNM used a cropped rectilinear domain and did not include the buffer regions, and because (as discussed above) the outer portions of the model domain have generally faster velocities due to the edge effects, this comparison is not valid. Therefore, to support more consistent comparison we ran a single STAR-CCM+ simulation using the cropped computational domain; the resulting breakthrough curve is also shown in Fig. 7. In this comparison, excellent agreement was achieved between the two models, although the particular PNM method used (*i.e.*, MCM) appears to be slightly more dispersive leading to a slightly lower peak.

4.2.2. Dispersion analysis

The macroscopic longitudinal dispersion coefficient can be estimated from the simulations for comparison. Here we used two methods to analyze the dispersion. For the simulation methods that performed transport simulations, the resulting breakthrough curves were fitted with a standard one-dimensional advection-dispersion model using the general solute transport model in STAMMT-L code [82]. We also used the method of volume averaging (MVA), solved numerically using the TETHYS code, to obtain estimates of dispersion coefficients corresponding to the simulated system. Richmond et al. [45] modified the MVA that it could be applied to unsteady cases (Section 3.1.1). The modified MVA has been previously validated for the simple cases of flow between parallel plates and tubes and was subsequently applied to a sinusoidal wavy tube problem and successfully compared with transport simulations based on a particle tracking method [45]. In the current study, MVA calculation was implemented in TETHYS and performed after flow and solute transport simulations.

The calculated Péclet ($\mathrm{Pe} = \mathrm{Sc} \times \mathrm{Re}$) number of the current sphere pack problem is 257. The apparent dispersion coefficient (D_L) computed by the MVA method is 1.66×10^{-6} m^2/s. The D_L fitted by STAMMT-L based on the breakthrough curves shown in Fig. 7 are 1.72×10^{-6} and 1.75×10^{-6} m^2/s for Star-CCM+ and TETHYS-40 μm-simulation (entire column). The results show good agreement between the modified MVA method and the values fitted to the 1D advection-dispersion equation.

5. Conclusions

We have performed comparative flow and solute transport simulations of an experimental porous medium using five different codes representing four general pore-scale modeling approaches. This is an extension of previous research that compared a single model approach with experimental data. This work also expands on previous studies by others in which multiple pore-scale simulators were compared in the context of a 2D system. The character of 3D flow and transport is significantly different that 2D in that additional degrees of freedom are available for flow and transport pathways, leading to potential differences in velocity patterns, degree of solute mixing, etc. The 3D complex pore geometry (randomly-packed spheres) used in the current study poses several additional challenges to numerical simulation, including: 1) accurate representation of the pore geometry; 2) meshing requirements; 3) convergence and stability issues; and 4) computing cost. Hence, it is a strong benchmark problem to test different pore-scale models, improve the performances and extend the capabilities of the computational codes. Although all the models represented the same model system to the degree possible, the methods varied widely in the degree of complexity of representation of the porous media geometry, the numerical algorithms used, mesh resolution and geometry, and computational requirements.

Quantitative comparisons are drawn in terms of microscopic measures (pore-scale velocities) and macroscopic measures (permeability, breakthrough curves, effective dispersivity). All models and codes gave broadly similar results in all categories, although there were some differences that may be deemed significant depending on the model context. Meshing and grid resolution were believed to be the major source of the differences. Comparisons of simulated tracer breakthrough were only performed for a subset of the codes that were capable of simulating solute transport. All obtained simulation results were in good agreement when differences in model configuration were properly accounted for, although some minor discrepancies were observed.

The computational demands of the various methods also varied widely, with some methods running in seconds on a single processor and others requiring hours or days on large supercomputers. The PNM in particular is highly computationally efficient, and therefore may be very well suited to rapid screening of alternatives or performing very large simulations in cases where slight overestimation of dispersive transport is not problematic. Of the class 1 models, the iRMB-LBM code executed on GPGPU was the most computationally efficient.

Additional analyses are needed to clearly identify the sources of the observed discrepancies (especially in the effective permeability), and further work is needed to enhance code capabilities to allow common comparison of transport simulations across the full suite of methods. However, in general we believe that this study provides a strong foundation for further development and application of pore-scale simulation methods to problems of porous media flow and transport. In order to share our knowledge and findings from the current study with the porous media flow research community and facilitate future extensions of this work, we will upload the benchmarking problem and our results to the PoreScaleBenchmark website: http://porescalebenchmark.pbworks.com/.

Acknowledgments

Research at Pacific Northwest National Laboratory (PNNL) was supported by the U. S. Department of Energy (DOE) Office of Biological and Environmental Research (BER) through the PNNL Subsurface Biogeochemical Research Scientific Focus Area project. Computations described here were performed using computational facilities of the Environmental Molecular Sciences Laboratory (EMSL), a national scientific user facility sponsored by DOE-BER and located at PNNL, computational facilities of PNNL's Institutional Computing program, and computational facilities of the National Energy Research Supercomputing Center, which is supported by the DOE Office of Science under Contract No. DE-AC02-05CH11231. PNNL is operated for the DOE by Battelle Memorial Institute under Contract No. DE-AC06-76RLO 1830.

Sandia National Laboratories is a multiprogram laboratory managed and operated by Sandia Corporation, a wholly owned subsidiary of Lockheed Martin Corporation, for the U.S. Department of Energy's National Nuclear Security Administration under contract DE-AC04-94AL85000. This SPH work was supported by the DOE Office of Science Advanced Scientific Computing Research (ASCR) Applied Mathematics program as part of the Collaboratory on Mathematics for Mesoscopic Modeling of Materials (CM4). This research used resources of the National Energy Research Scientific Computing Center, a DOE Office of Science User Facility supported by the Office of Science of the U.S. Department of Energy under Contract No. DE-AC02-05CH11231.

Institute for Computational Modelling in Civil Engineering (iRMB) at Technische Universität Braunschweig gratefully acknowledges financial support by the Deutsche Forschungsgemeinschaft (DFG) for funding the Research Training Group MUSIS (FOR 1083).

The pore-network modeling was carried out under funding from the Center for Frontiers of Subsurface Energy Security, an Energy Frontier Research Center funded by the U.S. Department of Energy, Office of Science, Office of Basic Energy Sciences, DOE Project No. DE-SC0001114. We would also like to thank Karsten Thompson and LSU for providing the network extraction algorithm.

References

[1] Bear J. Dynamics of fluids in porous media, New York: Dover Publications, Inc.; 1972. ISBN: 0-486-65675-6.

[2] Bear J, Cheng AH-D. Modeling groundwater flow and contaminant transport. Volume 23 of Theory and Applications of Transport in Porous Media. 1st. Dordrecht: Springer; 2010. http://dx.doi.org/10.1007/978-1-4020-6682-5.

[3] Suekane T, Yokouchi Y, Hirai S. Inertial flow structures in a simple-packed bed of spheres. AIChE J 2003;49(1):10–17. http://dx.doi.org/10.1002/aic.690490103.

[4] Nijemeisland M, Dixon AG. CFD study of fluid flow and wall heat transfer in a fixed bed of spheres. AIChE J 2004;50(5):906–21. http://dx.doi.org/10.1002/aic.10089.

[5] Gunjal PR, Ranade VV, Chaudhari RV. Computational study of a single-phase flow in packed beds of spheres. AIChE J 2005;51(2):365–78. http://dx.doi.org/10.1002/aic.10314.

[6] Maier RS, Kroll DM, Bernard RS, Howington SE, Peters JF, Davis HT. Enhanced dispersion in cylindrical packed beds. Philos Trans R Soc Lond Ser A — Math Phys Eng Sci 2002;360(1792):497–506. http://dx.doi.org/10.1098/rsta.2001.0951.

[7] Maier RS, Kroll DM, Bernard RS, Howington SE, Peters JF, Davis HT. Hydrodynamic dispersion in confined packed beds. Phys Fluids 2003;15(12):3795–815. http://dx.doi.org/10.1063/1.1624836.

[8] Maier RS, Schure MR, Gage JP, Seymour JD. Sensitivity of pore-scale dispersion to the construction of random bead packs. Water Resour Res 2008;44(6):W06S03. http://dx.doi.org/10.1029/2006wr005577.

[9] Oostrom M, Mehmani Y, Romero-Gomez P, Tang Y, Liu H, Yoon H, et al. Pore-scale and continuum simulations of solute transport micromodel benchmark experiments. Comput Geosci 2014:1–23. http://dx.doi.org/10.1007/s10596-014-9424-0.

[10] Battiato I, Tartakovsky DM, Tartakovsky AM, Scheibe TD. Hybrid models of reactive transport in porous and fractured media. Adv Water Resour 2011;34(9):1140–50. http://dx.doi.org/10.1016/j.advwatres.2011.01.012.

[11] Sun T, Mehmani Y, Balhoff MT. Hybrid multiscale modeling through direct substitution of pore-scale models into near-well reservoir simulators. Energy Fuels 2012;26(9):5828–36. http://dx.doi.org/10.1021/ef301003b.

[12] Scheibe TD, Murphy EM, Chen X, Rice AK, Carroll KC, Palmer BJ, et al. An analysis platform for multiscale hydrogeologic modeling with emphasis on hybrid multiscale methods. Groundwater 2015a;53(1):38–56. http://dx.doi.org/10.1111/gwat.12179.

[13] Scheibe TD, Schuchardt K, Agarwal K, Chase J, Yang X, Palmer BJ, et al. Hybrid multiscale simulation of a mixing-controlled reaction. Adv. Water Resour. 2015b;83:228–39. http://dx.doi.org/10.1016/j.advwatres.2015.06.006.

[14] Tang Y, Valocchi AJ, Werth CJ. A hybrid pore-scale and continuum-scale model for solute diffusion, reaction, and biofilm development in porous media. Water Resour Res 2015;51(3):1846–59. http://dx.doi.org/10.1002/2014wr016322.

[15] Valvatne PH, Piri M, Lopez X, Blunt MJ. Predictive pore-scale modeling of single and multiphase flow. Transp Porous Media 2005;58(1--2):23–41. http://dx.doi.org/10.1007/s11242-004-5468-2.

[16] Zaretskiy Y, Geiger S, Sorbie K, Forster M. Efficient flow and transport simulations in reconstructed 3D pore geometries. Adv Water Resour 2010;33(12):1508–16. http://dx.doi.org/10.1016/j.advwatres.2010.08.008.

[17] Tartakovsky AM, Meakin P, Scheibe TD, Wood BD. A smoothed particle hydrodynamics model for reactive transport and mineral precipitation in porous and fractured porous media. Water Resour Res 2007a;43(5):W05437. http://dx.doi.org/10.1029/2005wr004770.

[18] Wildenschild D, Sheppard AP. X-ray imaging and analysis techniques for quantifying pore-scale structure and processes in subsurface porous medium systems. Adv Water Resour 2013;51:217–46. http://dx.doi.org/10.1016/j.advwatres.2012.07.018.

[19] Seymour JD, Callaghan PT. Generalized approach to NMR analysis of flow and dispersion in porous media. AIChE J 1997;43(8):2096–111. http://dx.doi.org/10.1002/aic.690430817.

[20] Seymour JD, Codd SL, Gjersing EL, Stewart PS. Magnetic resonance microscopy of biofilm structure and impact on transport in a capillary bioreactor. J Mag Reson 2004a;167(2):322–7. http://dx.doi.org/10.1016/j.jmr.2004.01.009.

[21] Seymour JD, Gage JP, Codd SL, Gerlach R. Anomalous fluid transport in porous media induced by biofilm growth. Phys Rev Lett 2004b;93(19):198103. http://dx.doi.org/10.1103/PhysRevLett.93.198103.

[22] Seymour JD, Gage JP, Codd SL, Gerlach R. Magnetic resonance microscopy of biofouling induced scale dependent transport in porous media. Adv Water Resour 2007;30(6--7):1408–20. http://dx.doi.org/10.1016/j.advwatres.2006.05.029.

[23] Elkins CJ, Alley MT. Magnetic resonance velocimetry: applications of magnetic resonance imaging in the measurement of fluid motion. Exp Fluids 2007;43(6):823–58. http://dx.doi.org/10.1007/s00348-007-0383-2.

[24] Anderson JD. Computational fluid dynamics. McGraw-Hill Series in Mechanical Engineering. 1st. New York: McGraw-Hill; 1995. ISBN: 9780070016859.

[25] Yu D, Mei R, Luo L-S, Shyy W. Viscous flow computations with the method of lattice Boltzmann equation. Prog Aerosp Sci 2003;39(5):329–67. http://dx.doi.org/10.1016/S0376-0421(03)00003-4.

[26] Luo L-S, Krafczyk M, Shyy W. Lattice Boltzmann method for computational fluid dynamics. In: Blockley R, Shyy W, editors. Encyclopedia of arospace engineering. New York: Wiley; 2010. p. 651–60. ISBN: 9780470754405. chap. 56.

[27] Dellar P, Luo L-S. Lattice Boltzmann methods. In: Engquest B, editor. Encyclopedia of applied and computational mathematics. Berlin: Springer; 2015. Article 349, (in press).

[28] Monaghan JJ. Smoothed particle hydrodynamics. Annu Rev Astron Astrophys 1992;30:543–74. http://dx.doi.org/10.1146/annurev.aa.30.090192.002551.

[29] Bijeljic B, Blunt MJ. Pore-scale modeling of transverse dispersion in porous media. Water Resour Res 2007;43(12):W12S11. http://dx.doi.org/10.1029/2006wr005700.

[30] Yang XF, Scheibe TD, Richmond MC, Perkins WA, Vogt SJ, Codd SL, et al. Direct numerical simulation of pore-scale flow in a bead pack: comparison with magnetic resonance imaging observations. Adv Water Resour 2013;54:228–41. http://dx.doi.org/10.1016/j.advwatres.2013.01.009.

[31] Sukop MC, Huang H, Lin CL, Deo MD, Oh K, Miller JD. Distribution of multiphase fluids in porous media: Comparison between lattice Boltzmann modeling and micro-x-ray tomography. Phys Rev E 2008;77(2):026710. http://dx.doi.org/10.1103/PhysRevE.77.026710.

[32] Ahrenholz B, Tölke J, Krafczyk M. Lattice-Boltzmann simulations in reconstructed parametrized porous media. Int J Comput Fluid Dyn 2006;20(6):369–77. http://dx.doi.org/10.1080/10618560601024694.

[33] Ahrenholz B, Tölke J, Peters A PL, Krafczyk M, et al. Quantitative links between porous media structures and flow behavior across scales. Adv Water Resour 2008;31(9):1151–73. http://dx.doi.org/10.1016/j.advwatres.2008.03.009.

[34] Ahrenholz B, Niessner J, Helmig R, Krafczyk M. Pore-scale determination of parameters for macroscale modeling of evaporation processes in porous media. Water Resour Res 2011;47(7):W07543. http://dx.doi.org/10.1029/2010wr009519.

[35] Pan CX, Luo L-S, Miller CT. An evaluation of lattice Boltzmann schemes for porous medium flow simulation. Comput Fluids 2006;35(8--9):898–909. http://dx.doi.org/10.1016/j.compfluid.2005.03.008.

[36] Khirevich S, Ginzburg I, Tallarek U. Coarse- and fine-grid numerical behavior of MRT/TRT lattice-Boltzmann schemes in regular and random sphere packings. J Comput Phys 2015;281:708–42. http://dx.doi.org/10.1016/j.jcp.2014.10.038.

[37] Lucy LB. A numerical approach to the testing of the fission hypothesis. Astron J 1977;82:1013–24. http://dx.doi.org/10.1086/112164.

[38] Gingold RA, Monaghan JJ. Smoothed particle hydrodynamics — theory and application to non-spherical stars. Mon Not R Astron Soc 1977;181(2):375–89. http://dx.doi.org/10.1093/mnras/181.3.375.

[39] Tartakovsky AM, Meakin P, Scheibe TD, West RME. Simulations of reactive transport and precipitation with smoothed particle hydrodynamics. J Comput Phys 2007b;222(2):654–72. http://dx.doi.org/10.1016/j.jcp.2006.08.013.

[40] Tartakovsky A, Trask N, Pan K, Jones B, Pan W, Williams J. Smoothed particle hydrodynamics and its applications for multiphase flow and reactive transport in porous media. Comput Geosci 2015:1–28. http://dx.doi.org/10.1007/s10596-015-9468-9.

[41] Dong H, Blunt MJ. Pore-network extraction from micro-computerized-tomography images. Phys Rev E 2009;80(3):036307. http://dx.doi.org/10.1103/PhysRevE.80.036307.

[42] Mehmani Y, Oostrom M, Balhoff MT. A streamline splitting pore-network approach for computationally inexpensive and accurate simulation of transport in porous media. Water Resour Res 2014;50(3):2488–517. http://dx.doi.org/10.1002/2013wr014984.

[43] Mehmani Y, Balhoff MT. Mesoscale and hybrid models of fluid flow and solute transport. Rev Minerol Geochem 2015;80:433–59. http://dx.doi.org/10.2138/rmg.2015.80.13.

[44] Patankar SV. Numerical heat transfer and fluid flow, Washington, DC: Hemisphere; 1980. ISBN: 9780891165224.

[45] Richmond MC, Perkins WA, Scheibe TD, Lambert A, Wood BD. Flow and axial dispersion in a sinusoidal-walled tube: effects of inertial and unsteady flows. Adv Water Resour 2013;62:215–26. http://dx.doi.org/10.1016/j.advwatres.2013.06.014.

[46] Scheibe TD, Perkins WA, Richmond MC, McKinley MI, Romero-Gomez PDJ, Oostrom M, et al. Pore-scale and multiscale numerical simulation of flow and transport in a laboratory-scale column. Water Resour Res 2015c;51(2):1023–35. http://dx.doi.org/10.1002/2014wr015959.

[47] Ferziger JH, Perić M. Computational methods for fluid dynamics. 3rd. New York: Springer; 2001. http://dx.doi.org/10.1007/978-3-642-56026-2.

[48] Darwish MS, Moukalled F. TVD schemes for unstructured grids. Int J Heat Mass Transf 2003;46(4):599–611. http://dx.doi.org/10.1016/S0017-9310(02)00330-7.

[49] van Leer B. Towards the ultimate conservative difference scheme V. A second order sequel to Godunov's method. J Comput Phys 1979;32:101–36. http://dx.doi.org/10.1016/0021-9991(79)90145-1.

[50] Carbonell RG, Whitaker S. Dispersion in pulsed systems 2. Theoretical developments for passive dispersion in porous-media. Chem Eng Sci 1983;38(11):1795–802. http://dx.doi.org/10.1016/0009-2509(83)85036-2.

[51] Whitaker S. The method of volume averaging, Dordrecht: Kluwer Academic Publishers; 1999. ISBN: 9789401733892.

[52] Wood BD. Inertial effects in dispersion in porous media. Water Resour Res 2007;43(12):W12S16. http://dx.doi.org/10.1029/2006wr005790.

[53] Geier M, Schönherr M, Pasquali A, Krafczyk M. The cumulant lattice Boltzmann equation in three dimensions: theory and validation. Comput Math Appl 2015;70(4):507–47. http://dx.doi.org/10.1016/j.camwa.2015.05.001.

[54] He X, Luo L-S. A priori derivation of the lattice Boltzmann equation. Phys Rev E 1997a;55(6):R6333–6. http://dx.doi.org/10.1103/PhysRevE.55.R6333.

[55] He X, Luo L-S. Theory of the lattice Boltzmann method: from the Boltzmann equation to the lattice Boltzmann equation. Phys Rev E 1997b;56(6):6811–17. http://dx.doi.org/10.1103/PhysRevE.56.6811.

[56] He X, Luo L-S. Lattice Boltzmann model for the incompressible Navier–Stokes equation. J Stat Phys 1997c;88(3/4):927–44. http://dx.doi.org/10.1023/B:JOSS.0000015179.12689.e4.

[57] d'Humières D. Generalized lattice-Boltzmann equations. In: Shizgal BD, Weave DP, editors. Rarefied gas dynamics: theory and simulations. Volume 159 of Prog. Astronaut. Aeronaut. Washington, D.C.: AIAA; 1992. p. 450–8. http://dx.doi.org/10.2514/5.9781600866319.0450.0458.

[58] Lallemand P, Luo L-S. Theory of the lattice Boltzmann method: dispersion, dissipation, isotropy, Galilean invariance, and stability. Phys Rev E 2000;61(6):6546–62. http://dx.doi.org/10.1103/PhysRevE.61.6546.

[59] d'Humières D, Ginzburg I, Krafczyk M, Lallemand P, Luo L-S. Multiple-relaxation-time lattice Boltzmann models in three-dimensions. Philos Trans R Soc Lond Ser A 2002;360(1792):437–51. http://dx.doi.org/10.1098/rsta.2001.0955.

[60] Ginzburg I, Silva G, Talon L. Analysis and improvement of Brinkman lattice Boltzmann schemes: Bulk, boundary, interface. Similarity and distinctness with finite elements in heterogeneous porous media. Phys Rev E 2015;91(2):023307. http://dx.doi.org/10.1103/PhysRevE.91.023307.

[61] Bouzidi M, Firdaouss M, Lallemand P. Momentum transfer of Boltzmann-lattice fluid with boundaries. Phys Fluids 2001;13(11):3452–9. http://dx.doi.org/10.1063/1.1399290.

[62] Ginzburg I, d'Humières D. Multireflection boundary conditions for lattice Boltzmann models. Phys Rev E 2003;68(6):066614. http://dx.doi.org/10.1103/PhysRevE.68.066614.

[63] Linxweiler J, Krafczyk M, Tölke J. Highly interactive computational steering for coupled 3D flow problems utilizing multiple GPUs. Comput Vis Sci 2010;13(7):299–314. http://dx.doi.org/10.1007/s00791-010-0151-3.

[64] Trask N, Maxey M, Kim K, Perego M, Parks ML, Yang K, et al. A scalable consistent second-order SPH solver for unsteady low Reynolds number flows. Comput Methods Appl Mech Eng 2015;289:155–78. http://dx.doi.org/10.1016/j.cma.2014.12.027.

[65] Plimpton S. Fast parallel algorithms for short-range molecular dynamics. J Comput Phys 1995;117(1):1–19. http://dx.doi.org/10.1006/jcph.1995.1039.

[66] Heroux MA, Bartlett RA, Howle VE, Hoekstra RJ, Hu JJ, Kolda TG, et al. An overview of the trilinos project. ACM Trans Math Softw 2005;31(3):397–423. http://dx.doi.org/10.1145/1089014.1089021.

[67] Heroux MA. Epetra performance optimization guide. Sandia National Laboratories; 2009. SAND2009-1668.

[68] Bavier E, M H, Rajamanickam S, Thornquist H. Amesos2 and belos: direct and iterative solvers for large sparse linear systems. Sci Program 2012;20(3). http://dx.doi.org/10.3233/Spr-2012-0352.

[69] Gee MW, Siefert CM, Hu JJ, Tuminaro RS, Sala MG. ML 5.0 smoothed aggregation user's guide. Sandia National Laboratories; 2006. SAND2006-2649.

[70] Courant R, Friedrichs K, Lewy H. On the partial differential equations of mathematical physics. Math Ann 1928;100(1):32–74. http://dx.doi.org/10.1007/Bf01448839.

[71] Holmes DW, Williams JR, Tilke P. Smooth particle hydrodynamics simulations of low reynolds number flows through porous media. Int J Numer Anal Methods Geomech 2011;35(4):419–37. http://dx.doi.org/10.1002/nag.898.

[72] Morris JP, Fox PJ, Zhu Y. Modeling low Reynolds number incompressible flow using SPH. J Comput Phys 1997;136(1):214–26. http://dx.doi.org/10.1006/jcph.1997.5776.

[73] Mehmani Y. Modeling single-phase flow and solute transport across scales (Ph.D. thesis). University of Texas Austin; 2014.

[74] Acharya RC, van der Zee S, Leijnse A. Transport modeling of nonlinearly adsorbing solutes in physically heterogeneous pore networks. Water Resour Res 2005;41(2):W02020. http://dx.doi.org/10.1029/2004wr003500.

[75] Mehmani Y, Sun T, Balhoff MT, Eichhubl P, Bryant S. Multiblock pore-scale modeling and upscaling of reactive transport: Application to carbon sequestration. Transport Porous Media 2012;95(2):305–26. http://dx.doi.org/10.1007/s11242-012-0044-7.

[76] Mehmani Y, Balhoff MT. Pore-network modeling of longitudinal dispersion (in preparation).

[77] Thompson KE, Willson CS, White CD, Nyman SL, Bhattacharya JP, Reed AH. Application of a new grain-based reconstruction algorithm to microtomography images for quantitative characterization and flow modeling. SPE J 2008;13(2):164–76. http://dx.doi.org/10.2118/95887-PA.

[78] Patzek TW, Silin DB. Shape factor and hydraulic conductance in noncircular capillaries I. One-phase creeping flow. J Colloid Interface Sci 2001;236(2):295–304. http://dx.doi.org/10.1006/jcis.2000.7413.

[79] Eisfeld B, Schnitzlein K. The influence of confining walls on the pressure drop in packed beds. Chem Eng Sci 2001;56(14):4321–9. http://dx.doi.org/10.1016/S0009-2509(00)00533-9.

[80] Reichelt W. Calculation of pressure-drop in spherical and cylindrical packings for single-phase flow. Chemie Ingenieur Technik 1972;44(18):1068–73. http://dx.doi.org/10.1002/cite.330441806.

[81] Carman PC. Fluid flow through granular beds. Trans Inst Chem Eng 1937;15:150–66.

[82] Haggerty R. Reeves PC. STAMMT-L Version 1.0 User's Manual. Sandia National Laboratories; 2002. ERMS 520308-76.